GEOPHYSICAL RESEARCH LETTERS, VOL. 38, L02202, doi:10.1029/2010GL045302, 2011

Thrust faults and the near-surface strength of asteroid 433 Eros

Thomas R. Watters,[1] Peter C. Thomas,[2] and Mark S. Robinson[3]

Received 27 August 2010; revised 9 November 2010; accepted 23 November 2010; published 22 January 2011.

[1] NEAR Shoemaker images reveal widespread occurrence of tectonic landforms on asteroid 433 Eros. Hinks Dorsum is a ridge that extends for about 18 km around the asteroid and strongly resembles thrust fault structures on the terrestrial planets. Tectonic landforms can provide information on the mechanical properties of asteroids, a subject of much controversy. Modeling constrained by topographic data shows that Hinks Dorsum can be accounted for by a shallow rooted thrust fault no greater than 250 m in depth with ~90 m of cumulative slip. Strength envelopes based on frictional and rock mass strength criteria suggest the near-surface shear strength of Eros is from ~1 to 6 MPa. A spatial correlation is found between Shoemaker crater, a transition from low to high crater density, and Hinks Dorsum. This spatial relation along with the estimated strength of the asteroid suggests the thrust fault was formed by impact induced compression. **Citation:** Watters, T. R., P. C. Thomas, and M. S. Robinson (2011), Thrust faults and the near-surface strength of asteroid 433 Eros, *Geophys. Res. Lett.*, *38*, L02202, doi:10.1029/2010GL045302.

1. Introduction

[2] Eros is a near-Earth, S-type asteroid that comes within 0.13 astronomical units of Earth's orbit [*Veverka et al.*, 2000]. It is an elongated body measuring roughly 34 km by 11 km by 11 km [*Veverka et al.*, 2000]. The NEAR Shoemaker spacecraft orbited Eros for a year before it became the first spacecraft to land on an asteroid [*Veverka et al.*, 2001a]. The multispectral imager (MSI) obtained 5 m/pixel or better resolution images of the entire surface and acquired hundreds of images with sub-meter pixel scales [*Veverka et al.*, 2001b]. The shape of the asteroid was determined from image-based techniques [*Thomas et al.*, 2002a] and laser ranging from the NEAR Laser Rangefinder (NLR) [*Zuber et al.*, 2000; *Miller et al.*, 2002]. NLR profiles resolve small-scale landforms with only a few meters of relief [*Cheng et al.*, 2001, 2002].

[3] Hinks Dorsum (also informally called Rahe Dorsum) consists of a series of segments that are typically asymmetric in cross-section (Figure 1) [*Veverka et al.*, 2000; *Cheng et al.*, 2001; *Prockter et al.*, 2002; *Thomas et al.*, 2002b; *Thomas and Prockter*, 2010]. The easternmost terminus of Hinks Dorsum is marked by a series of scarps and troughs located on the slopes of Himeros [*Veverka et al.*, 2000; *Prockter et al.*, 2002]. Crosscutting relationships, the lack of superimposed impact craters, and the relatively pristine appearance of Hinks Dorsum led to the conclusion that it is a relatively young structure that formed after Eros had evolved into its present shape [*Veverka et al.*, 2000].

2. Topography of Hinks Dorsum

[4] Hinks Dorsum is similar in morphology to lobate scarps found on Mercury and Mars [cf. *Watters*, 2003; *Watters et al.*, 2009], and it is similar in scale to lunar lobate scarps [cf. *Watters et al.*, 2010]. Lobate scarps on the Moon, Mercury and Mars often cut and offset the walls and floors of impact craters and are interpreted to be the surface expressions of thrust faults [*Watters*, 2003; *Watters et al.*, 2002, 2009, 2010]. Topographic profiles derived from NLR data confirm that the cross-sectional geometry of Hinks Dorsum is weakly to strongly asymmetric [also see *Cheng et al.*, 2002] with the vergent side to the north (Figure 1). The segments of Hinks Dorsum near Tutanekai crater have a maximum relief of ~60 m (Figures 1 and 2a). Image and topographic data reveal two smaller subsidiary scarps flanking Hinks Dorsum (Figure 1). The smaller of the subsidiary scarps has a maximum relief of about 25 m (Figure 2b), while the larger scarp has about 50 m of relief. Measured slopes of the northern, vergent-side of Hinks Dorsum and the secondary scarp are ~20°, comparable to maximum slopes of scarp faces of large-scale lobate scarps on Mercury and Mars [*Watters*, 2003; *Watters et al.*, 1998]. An analysis of topographic profiles across the segment of Hinks Dorsum in Himeros indicates the northern side is also the vergent, steeper-side of the scarp. The consistent northward vergence suggests the underlying thrust fault extends below the southern flanks of Hinks Dorsum along its entire length.

3. Modeling

[5] We simulated deformation over a thrust fault that propagates upward toward the surface using elastic dislocation modeling [*Lin and Stein*, 2004; *Toda et al.*, 2005]. The magnitude and sense of slip is specified, and the stresses and material displacements are determined using the stress functions for an elastic half-space [*Okada*, 1992]. The fault surface is defined as a rectangular plane having a dip (θ), and vertical depth of faulting (T_1, T_2) (Figure 2c). We assumed that deformation occurred above a blind thrust fault (non-surface breaking) because there is no photogeologic evidence of vertical offset at the base of the vergent side (scarp face) of Hinks Dorsum. We estimated the magnitude of the slip D from the height of the scarp

[1] Center for Earth and Planetary Studies, National Air and Space Museum, Smithsonian Institution, Washington, D. C., USA.
[2] Center for Radiophysics and Space Research, Cornell University, Ithaca, New York, USA.
[3] School of Earth and Space Exploration, Arizona State University, Tempe, Arizona, USA.

0094-8276/11/2010GL045302

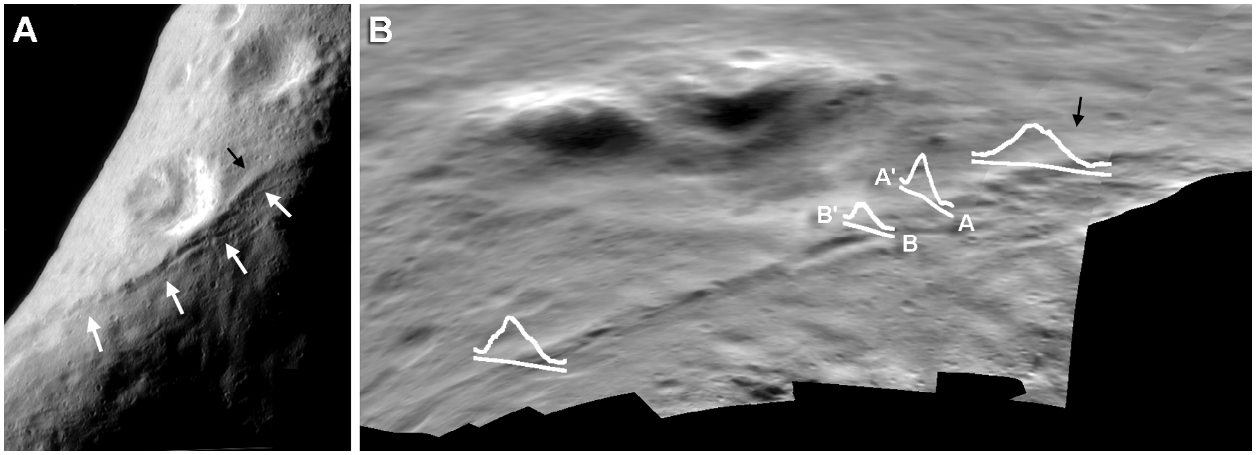

Figure 1. Hinks Dorsum on Eros. (a) The MSI mosaic shows the western segments of Hinks Dorsum (arrows). Hinks occurs near the rim the crater Tutanekai and is flanked by two smaller subsidiary ridges. Black arrow indicates the location of a debris apron. (b) MSI mosaic in simple cylindrical projection with the locations of topographic profiles derived from NLR data. Topographic profiles are plotted above the profile location lines with a large vertical exaggeration. Profiles were generated by converting radius data into geopotential heights [*Cheng et al.*, 2002] and detrended relative to an arbitrary datum. Black arrow indicates the location of the same debris apron shown in Figure 1a. The mosaic covers the area from 30°N to 70°N and 315°W to 35°W.

and then adjusted D, along with the other free parameters, until the best fit with the topography was achieved. The relative-slip distribution along the model fault is tapered with the minimum slip at the fault tips. Although the geometry and depth of faulting cannot be uniquely determined, the modeling gives a good fit to the topography within a relatively narrow range of parameters [see *Watters et al.*, 2002].

[6] Modeling of Hinks Dorsum suggests the underlying fault has a dip of ~40°, a maximum depth of ~240 m, and a slip of ~90 m (Figure 2a). Modeling of one of the secondary ridges indicates an underlying fault with a dip of ~35°, a maximum depth of ~200 m, and a slip of ~40 m (Figure 2b). These estimates suggest that Hinks Dorsum and the secondary ridges are the surface expression of shallow-rooted thrust faults with thrust slip directions to the north.

[7] Because the modeling is constrained by topography, factors such as the orientation of the orbital track relative to the strike of Hinks Dorsum or post-deformation modification of the structure will influence the model results. NLR data tracks rarely cross segments of Hinks Dorsum at the optimal angle (perpendicular to its orientation) (Figure 1b). The orientation of the profiles used to constrain the modeling, however, are nearly orthogonal to the scarp segments (Figures 1b and 2) and thus, minimize the error. Evidence of downslope movement or slumping on the vergent-side of the scarp indicates that the post-deformation slopes of Hinks Dorsum have been modified (Figure 1). Relatively high albedo material appears to have moved down the slope of the scarp face forming debris aprons on the foot wall-side of some segments (Figure 1). Debris aprons from downslope regolith movement are common on Eros [see *Robinson et al.*, 2002]. The slope of the scarp face strongly influences the best-fit depth of the upper fault tip T_1. Thus, it is possible that the depth of the upper tip of the blind thrust fault is nearer to the surface than the best-fit value would suggest. However, there is no evidence of debris aprons on the segments modeled (Figure 1b).

4. Stresses and Strength

[8] The origin of the compressional stresses that formed Hinks Dorsum is not well understood. Surveys of tectonic features on Eros show only a few sets of structures radial to impact or other features [*Prockter et al.*, 2002; *Thomas et al.*, 2002b; *Buczkowski et al.*, 2008]. Impact craters with squared outlines, however, are cited as evidence of structural control [*Cheng et al.*, 2002; *Prockter et al.*, 2002]. The global distribution of grooves, troughs, and ridges on Eros suggests a pervasive fabric of fractures [*Prockter et al.*, 2002; *Thomas et al.*, 2002b], supporting the interpretation that the asteroid is a coherent body held together by material strength rather than by gravitational attraction alone [*Zuber et al.*, 2000; *Prockter et al.*, 2002; *Thomas et al.*, 2002b]. Proposed expressions of this fabric are a Calisto Fossae-Hinks Dorsum plane and a prominent facet of Eros [see *Thomas et al.*, 2002b]. Our analysis indicates that the dip of the Hinks Dorsum fault is not along these planes and thus the fault was likely not influenced by the putative fabric. This does not exclude the possibility that the Hinks Dorsum fault exploited another preexisting zone of weakness, conjugate to the Calisto and surface facet planes.

[9] The stress necessary to initiate thrust faulting on Eros is determined by its near-surface strength. Two approaches are used to evaluate the near-surface shear strength of the asteroid, frictional strength and rock mass strength. The frictional strength is controlled by the resistance to brittle failure by sliding on randomly oriented, through going fractures (Byerlee's law). In terms of the maximum σ_1 and minimum σ_3 principal effective stresses Byerlee's law is expressed by $\sigma_1 \simeq 5\sigma_3$ for $\sigma_3 < 110$ MPa where $\sigma_3 = \rho g z$ and ρ is the density, g acceleration due to gravity, and z is the depth [see *Brace and Kohlstedt*, 1980]. Although g on Eros varies from 0.24 to 0.56 cm s^{-2} [*Veverka et al.*, 2001a],

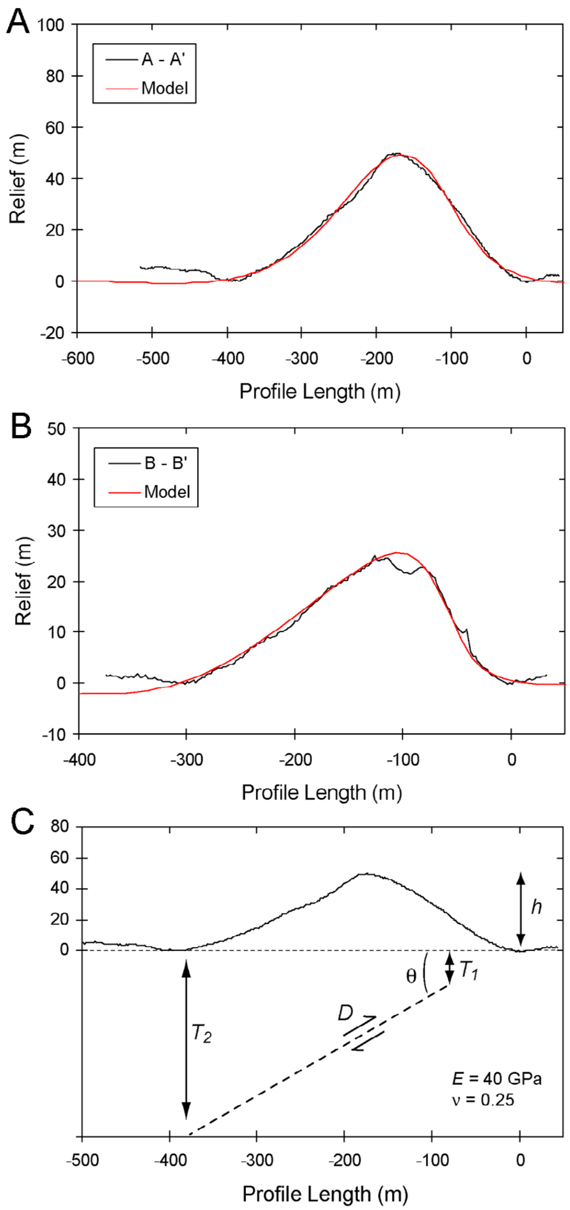

Figure 2. Topographic profiles across Hinks Dorsum. (a) The profiles were generated by converting radius data into geopotential heights and then detrended to an arbitrary datum. The predicted structural relief is for an elastic dislocation model with $\theta = 43°$, $T_2 = 240$ m, and $D = 93$ m. Vertical exaggeration is ~4:1. (b) Topographic profile across a subsidiary ridge flanking Hinks Dorsum. The predicted structural relief is for a model with $\theta = 35°$, $T_2 = 190$ m, and $D = 40$ m. Profile locations are shown in Figure 1b and the vertical exaggeration is ~5:1. (c) Model parameters are the depth of the upper T_1 and lower T_2 tip, the fault plane dip angle θ, and the slip D. The values of Young's modulus E and Poisson's ratio ν of the elastic half-space are shown. The topographic profiles are the same shown in Figure 2a. The vertical exaggeration is ~2:1. The depth of faulting is not to scale.

0.5 cm s^{-2} is a good average in the area of Hinks Dorsum [see *Robinson et al.*, 2001, Figure 2]. Using the mean density of Eros $\rho = 2.67$ g/cm^2 [*Veverka et al.*, 2000], the shear strength at a depth of 0.25 km is ~1.3 MPa (Figure 3). The frictional strength criteria is a lower limit on the shear strength for near-surface rocks because it assumes the cohesion $C_o = 0$ [see *Schultz*, 1993; *Scholz*, 2002]. The strength of near-surface rocks with non-zero cohesion is better represented by the Hoek-Brown failure criterion given by

$$\sigma_1 = \sigma_3 + \sigma_c \left(m \frac{\sigma_3}{\sigma_c} + s \right)^a \tag{1}$$

where σ_1 and σ_3 are the effective principal stresses, σ_c is the uniaxial compressive strength of intact rock, and m, s, and a are material constants related to the Geologic Strength Index (GSI) and a rock mass disturbance factor d [*Hoek et al.*, 2002; *Hoek and Diederichs*, 2006]. Using $\sigma_c = 200$ MPa, the mean compressive strength of intact stony meteorites [*Petrovic*, 2001], a GSI = 45 (consistent with highly jointed basalt rock mass), and $d = 1.0$ (where 0 = undisturbed, 1 = very disturbed) [*Hoek et al.*, 2002], the shear strength at a depth of 0.25 km is ~6 MPa (Figure 3). Based on these two approaches, we estimate the near-surface shear strength of Eros to be from ~1 to 6 MPa. This shear strength is well above the maximum expected from tidally induced stresses [e.g., *Dobrovolskis*, 1982] and far exceeds recent estimates of the strength of Phobos, Pandora, and Epimetheus (0.01 to 0.1 MPa) [*Morrison et al.*, 2009]. Thermally induced stresses could exceed 5 MPa [*Dombard and Freed*, 2002], however, the presence of a relatively thick, uncompacted regolith [*Veverka et al.*, 2001b; *Robinson et al.*, 2002; *Thomas and Robinson*, 2005] will likely insolate the interior from their effects. The most likely source of stress capable of forming thrust faults on Eros is impact-induced compression [*Melosh*, 1989; *Richardson et al.*, 2004; *Thomas et al.*, 2001].

[10] The relatively young impact crater Shoemaker (there is no IAU approved name for this crater), which contains Charlois Regio, is ~7.6 km in diameter and is superposed on the rim of the larger Himeros crater [*Thomas et al.*, 2002a; *Thomas and Robinson*, 2005]. The relatively young age of both Shoemaker crater and Hinks Dorsum, combined with the likely need for impact-induced stress in the formation of Hinks, raises the question of a possible genetic relation. Shoemaker has been associated with most of the large ejecta blocks on Eros [*Thomas et al.*, 2001], and has removed

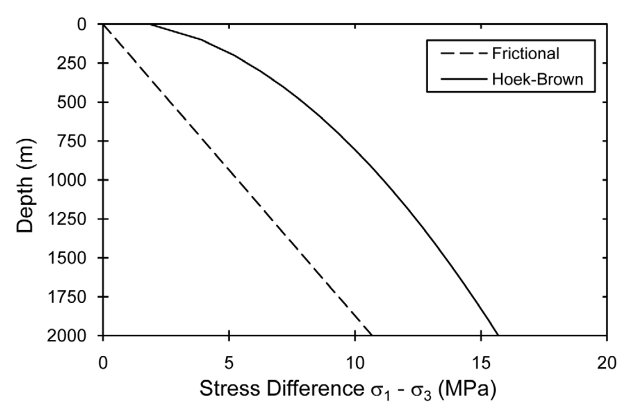

Figure 3. Strength envelops for the near-surface of Eros. The frictional strength was determined using Byerlee's law. The Hoek-Brown strength envelop was determined using equation (1) with material constants consistent with a partially disrupted, highly jointed basalt rock mass.

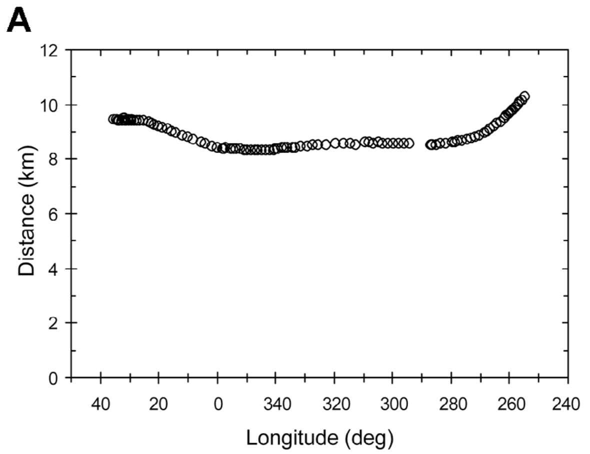

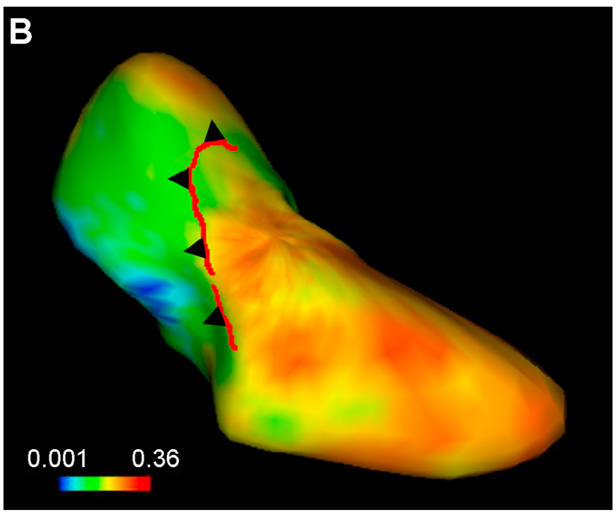

Figure 4. Distance and crater density relative to Shoemaker crater. (a) Straight-line distance through Eros from the center of Shoemaker crater to Hinks Dorsum as a function of longitude. Over half of the length of Hinks Dorsum is within 8.3 to 8.6 km from the center of Shoemaker. (b) Color-coded crater densities on Eros. Crater density data are binned between diameters of 0.177 to 1 km with color values scaled to the log of the R-value [*Thomas and Robinson*, 2005]. The location of Hinks Dorsum is shown (red line). The dip direction of the Hinks Dorsum thrust fault inferred from the vergence of the scarp is indicated by black triangles.

much of the population of craters <0.5 km in diameter within ~9 km straight line distance of the center of Shoemaker [*Thomas and Robinson*, 2005]. A global structural feature map of Eros shows that Hinks Dorsum is roughly circumferential to the center of Shoemaker [see *Thomas et al.*, 2002b, Figure 1], and the northward thrust slip direction of the fault is away from the crater center. Following the approach of *Thomas and Robinson* [2005], the straight-line distance from the center of Shoemaker to points along Hinks Dorsum are plotted (Figure 4a). The plot indicates that Hinks Dorsum has a simple geometric relation to Shoemaker crater. Over half its length is within a very narrow range of distance from the center of Shoemaker (~8.3 to 8.6 km), with a maximum distance of ~10.3 km at the eastern end of the structure (Figure 4a). While the loss of craters within a certain distance of Shoemaker can be related to a level of impact induced acceleration or energy deposition, the formation of a thrust fault at a near-constant distance may have involved compressional stresses that exceeded 6 MPa. We note that segments of Hinks Dorsum are very close to the transition from low to high crater density, particularly in Himeros (Figure 4b). This spatial correlation suggests that the Hinks Dorsum thrust faults acted as a mechanical discontinuity where seismic shaking was attenuated. The crater density effects reach ~9 km from Shoemaker around the entire asteroid, so any discontinuity at Hinks is not the only control on the crater density transition. Impact-induced compression from the Shoemaker event may have formed the Hinks Dorsum thrust fault, and subsequent seismic shaking likely resulted in the additional slip on the fault and the growth of the structure.

[11] **Acknowledgments.** We thank the two anonymous reviewers for helpful comments that improved the manuscript. This work is supported by the National Aeronautics and Space Administration under grants issued through the Office of the Planetary Geology and Geophysics Program.

References

Brace, W. F., and D. L. Kohlstedt (1980), Limits on lithospheric stress imposed by laboratory experiments, *J. Geophys. Res.*, *85*, 6248–6252, doi:10.1029/JB085iB11p06248.

Buczkowski, D. L., O. S. Barnouin-Jha, and L. M. Prockter (2008), 433 Eros lineaments: Global mapping and analysis, *Icarus*, *193*, 39–52, doi:10.1016/j.icarus.2007.06.028.

Cheng, A. F., et al. (2001), Laser altimetry of small-scale features on 433 Eros from NEAR-Shoemaker, *Science*, *292*, 488–491, doi:10.1126/science.1058330.

Cheng, A. F., et al. (2002), Small scale topography of 433 Eros from laser altimetry and imaging, *Icarus*, *155*, 51–74, doi:10.1006/icar.2001.6750.

Dobrovolskis, A. (1982), Internal stresses in Phobos and other triaxial bodies, *Icarus*, *52*, 136–148, doi:10.1016/0019-1035(82)90174-9.

Dombard, A. J., and A. M. Freed (2002), Thermally induced lineations on the asteroid Eros: Evidence of orbit transfer, *Geophys. Res. Lett.*, *29*(16), 1818, doi:10.1029/2002GL015181.

Hoek, E., and M. S. Diederichs (2006), Empirical estimation of rock mass modulus, *Int. J. Rock Mech. Min. Sci.*, *43*, 203–215, doi:10.1016/j.ijrmms.2005.06.005.

Hoek, E., C. T. Carranza-Torres, and B. Corkum (2002), Hoek-Brown criterion, in *Proceedings 5th North American Rock Mechanics Symposium*, edited by R. P. Young, pp. 267–273, Toronto, Ont., Canada.

Lin, J., and R. S. Stein (2004), Stress triggering in thrust and subduction earthquakes, and stress interaction between the southern San Andreas and nearby thrust and strike-slip faults, *J. Geophys. Res.*, *109*, B02303, doi:10.1029/2003JB002607.

Melosh, H. J. (1989), *Impact Cratering*, 245 pp., Oxford Univ. Press, New York.

Miller, J. K., et al. (2002), Determination of shape, gravity, and rotational state of asteroid 433 Eros, *Icarus*, *155*, 3–17, doi:10.1006/icar.2001.6753.

Morrison, S. J., P. C. Thomas, M. S. Tiscareno, J. A. Burns, and J. Veverka (2009), Grooves on small saturnian satellites and other objects: Characteristics and significance, *Icarus*, *204*, 262–270, doi:10.1016/j.icarus.2009.06.003.

Okada, Y. (1992), Internal deformation due to shear and tensile faults in a half-space, *Bull. Seismol. Soc. Am.*, *82*, 1018–1040.

Petrovic, J. J. (2001), Review mechanical properties of meteorites and their constituents, *J. Mater. Sci.*, *36*, 1579–1583, doi:10.1023/A:1017546429094.

Prockter, L., et al. (2002), Surface expressions of structural features on Eros, *Icarus*, *155*, 75–93, doi:10.1006/icar.2001.6770.

Richardson, J. E., H. J. Melosh, and R. Greenberg (2004), Impact-induced seismic activity on asteroid 433 Eros: A surface modification process, *Science*, *306*, 1526–1529, doi:10.1126/science.1104731.

Robinson, M. S., P. C. Thomas, J. Veverka, S. Murchie, and B. Carcich (2001), The nature of ponded deposits on Eros, *Nature*, *413*, 396–400, doi:10.1038/35096518.

Robinson, M. S., P. C. Thomas, J. Veverka, S. Murchie, and B. B. Wilcox (2002), The geology of Eros, *Meteorit. Planet. Sci.*, *37*, 1651–1684, doi:10.1111/j.1945-5100.2002.tb01157.x.

Scholz, C. H. (2002), *The Mechanics of Earthquakes and Faulting*, pp. 53–100, Cambridge Univ. Press, Cambridge, U. K.

Schultz, R. A. (1993), Brittle strength of basaltic rock masses with applications to Venus, *J. Geophys. Res.*, *98*, 10,883–10,895, doi:10.1029/93JE00691.

Thomas, P. C., and L. M. Prockter (2010), Tectonics of small bodies, in *Planetary Tectonics*, edited by T. R. Watters and R. A. Schultz, pp. 233–263, Cambridge Univ. Press, New York.

Thomas, P. C., and M. S. Robinson (2005), Seismic resurfacing by a single impact on the asteroid 433 Eros, *Nature*, *436*, 366–369, doi:10.1038/nature03855.

Thomas, P. C., et al. (2001), Shoemaker crater as the source of most ejecta blocks on the asteroid 433 Eros, *Nature*, *413*, 394–396, doi:10.1038/35096513.

Thomas, P. C., et al. (2002a), Eros: Shape, topography and slope processes, *Icarus*, *155*, 18–37, doi:10.1006/icar.2001.6755.

Thomas, P. C., et al. (2002b), Global structure of asteroid 433 Eros, *Geophys. Res. Lett.*, *29*(10), 1408, doi:10.1029/2001GL014599.

Toda, S., R. S. Stein, K. Richards-Dinger, and S. Bozkurt (2005), Forecasting the evolution of seismicity in southern California: Animations built on earthquake stress transfer, *J. Geophys. Res.*, *110*, B05S16, doi:10.1029/2004JB003415.

Veverka, J., et al. (2000), Near at Eros: Imaging and spectral results, *Science*, *289*, 2088–2097, doi:10.1126/science.289.5487.2088.

Veverka, J., et al. (2001a), The landing of the NEAR-Shoemaker spacecraft on asteroid 433 Eros, *Nature*, *413*, 390–393, doi:10.1038/35096507.

Veverka, J., et al. (2001b), Imaging of small-scale features on 433 Eros from NEAR: Evidence for a complex regolith, *Science*, *292*, 484–488, doi:10.1126/science.1058651.

Watters, T. R. (2003), Thrust faulting along the dichotomy boundary in the eastern hemisphere of Mars, *J. Geophys. Res.*, *108*(E6), 5054, doi:10.1029/2002JE001934.

Watters, T. R., M. S. Robinson, and A. C. Cook (1998), Topography of lobate scarps on Mercury: New constraints on the planet's contraction, *Geology*, *26*, 991–994, doi:10.1130/0091-7613(1998)026<0991:TOLSOM>2.3.CO;2.

Watters, T. R., R. A. Schultz, M. S. Robinson, and A. C. Cook (2002), The mechanical and thermal structure of Mercury's early lithosphere, *Geophys. Res. Lett.*, *29*(11), 1542, doi:10.1029/2001GL014308.

Watters, T. R., S. C. Solomon, M. S. Robinson, J. W. Head, S. L. André, S. A. Hauck, and S. L. Murchie (2009), The tectonics of Mercury: The view after MESSENGER's first flyby, *Earth Planet. Sci. Lett.*, *285*, 283–296, doi:10.1016/j.epsl.2009.01.025.

Watters, T. R., et al. (2010), New evidence of recent thrust faulting on the Moon revealed by the Lunar Reconnaissance Orbiter Camera, *Science*, *329*, 936–940, doi:10.1126/science.1189590.

Zuber, M. T., et al. (2000), The shape of 433 Eros from the NEAR-Shoemaker Laser Rangefinder, *Science*, *289*, 2097–2101, doi:10.1126/science.289.5487.2097.

M. S. Robinson, School of Earth and Space Exploration, Arizona State University, Tempe, AZ 85251, USA.

P. C. Thomas, Center for Radiophysics and Space Research, Cornell University, 422 Space Sciences Bldg., Ithaca, NY 14853, USA.

T. R. Watters, Center for Earth and Planetary Studies, National Air and Space Museum, Smithsonian Institution, Washington, DC 20560-0315, USA. (watterst@si.edu)